

Measurements of  $B \rightarrow DK$  decays to constrain the CKM  
Unitarity Triangle angle  $\gamma$  and related results at LHCbDANIEL CRAIK <sup>1</sup>*Department of Physics  
University of Warwick, Coventry, UK*

Constraints on the CKM angle  $\gamma$  are presented from GLW, ADS, and GGSZ analyses of  $B^\pm \rightarrow DK^\pm$  at the LHCb experiment. The branching fractions of  $B^0 \rightarrow \bar{D}^0 K^+ \pi^-$  and  $B_s^0 \rightarrow \bar{D}^0 K^- \pi^+$  are also reported, measured relative to the related mode  $B^0 \rightarrow \bar{D}^0 \pi^+ \pi^-$ .

PRESENTED AT

DPF 2013

The Meeting of the American Physical Society  
Division of Particles and Fields  
Santa Cruz, California, August 13–17, 2013

---

<sup>1</sup>On behalf of the LHCb Collaboration.

# 1 Measurements of $\gamma$ from $B^\pm \rightarrow DK^\pm$

The CKM angle  $\gamma = \arg(-V_{ud}V_{ub}^*/V_{cd}V_{cb}^*)$  is currently the least well-constrained angle in the Unitarity Triangle. So far, the most-sensitive measurements of  $\gamma$  from a single experiment have been performed by Belle [1] and BaBar [2]. These measurements yield values of  $(68^{+15}_{-14})^\circ$  and  $(69^{+17}_{-16})^\circ$ , respectively.

Tree-level processes such as  $B^\pm \rightarrow DK^\pm$  provide a theoretically clean measurement of  $\gamma$  with no contributions from new physics processes. This measurement can be compared with measurements from loop-mediated processes, which are sensitive to new physics, to provide a test of the Standard Model. The current limits on the CKM Unitarity Triangle due to tree-level and loop processes, as calculated by the CKMFitter group [3], are shown in Fig. 1.

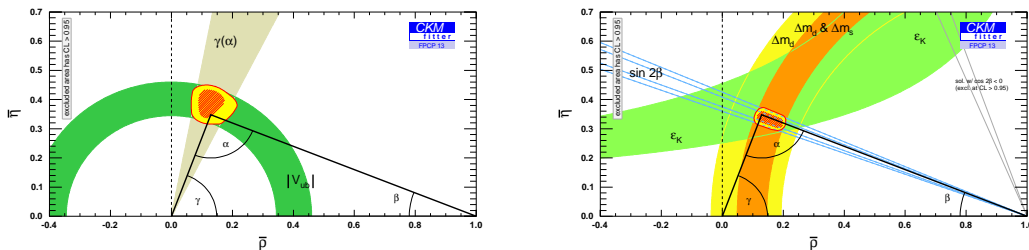


Figure 1: Constraints on the CKM Unitarity Triangle due to (left) tree-level processes and (right) loop-mediated processes.

## 1.1 GLW/ADS analysis of $B^\pm \rightarrow DK^\pm$ and $B^\pm \rightarrow D\pi^\pm$

The GLW method [4] uses  $D$  decays to  $CP$  eigenstates such as  $K^+K^-$  and  $\pi^+\pi^-$ . Decays can proceed either via a  $D^0$  or a  $\bar{D}^0$  with a phase difference of  $\delta_B + \gamma$ . Suppression in the decay via  $D^0$  with respect to the  $\bar{D}^0$  decay limits interference to  $\mathcal{O}(10\%)$  in  $B^\pm \rightarrow DK^\pm$  and  $\mathcal{O}(1\%)$  in  $B^\pm \rightarrow D\pi^\pm$ .

The ADS method [5] uses  $D$  decays to quasi-flavour-specific states such as  $\pi^+K^-$  and  $\pi^-K^+\pi^+\pi^-$ . Here the suppression of one of the  $B$  decays is partially balanced by the suppression of one of the  $D$  decays, giving larger interference terms while also introducing an additional phase shift of  $\delta_D$ .

Analyses have been performed on  $B^\pm \rightarrow DK^\pm$  and  $B^\pm \rightarrow D\pi^\pm$  with the  $D$  meson reconstructed from the final states  $K^+K^-$ ,  $\pi^+\pi^-$ ,  $K^+\pi^-$ ,  $\pi^+K^-$ ,  $K^-\pi^+\pi^+\pi^-$  and  $\pi^-K^+\pi^+\pi^-$  using LHCb data corresponding to  $1\text{fb}^{-1}$  of  $pp$  collisions at a centre of mass energy of 7 TeV [6, 7]. The invariant mass distributions of the two- and four-body suppressed ADS modes are shown in Fig. 2 and Fig. 3, respectively. The

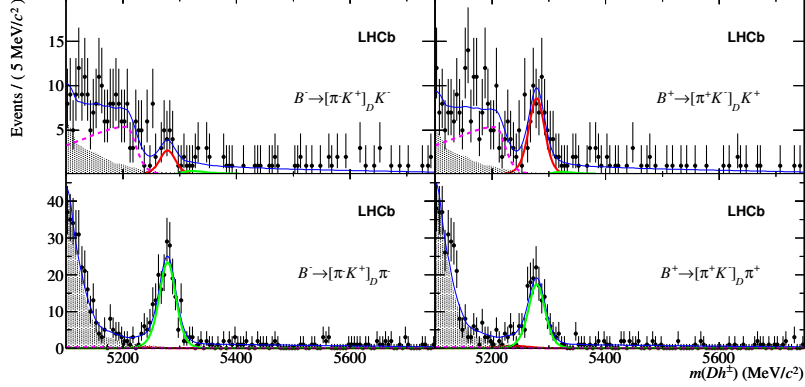


Figure 2: Fits to the invariant mass distributions of the two-body suppressed ADS mode  $\pi^\mp K^\pm$  in (top)  $B^\mp \rightarrow DK^\mp$  and (bottom)  $B^\mp \rightarrow D\pi^\mp$ . The  $B^\mp \rightarrow DK^\mp$  and  $B^\mp \rightarrow D\pi^\mp$  components are shown in red and green, respectively. The shaded component indicates partially reconstructed background, the dashed magenta line corresponds to partially reconstructed  $\Lambda_c^0 \rightarrow \Lambda_c^+ h^-$  and the total shape also includes a combinatoric background.

observables measured are the ratio of  $DK$  to  $D\pi$  for each  $D$  final state,

$$R_{K/\pi}^f = \frac{\Gamma(B^- \rightarrow D[\rightarrow f]K^-) + \Gamma(B^+ \rightarrow D[\rightarrow \bar{f}]K^+)}{\Gamma(B^- \rightarrow D[\rightarrow f]\pi^-) + \Gamma(B^+ \rightarrow D[\rightarrow \bar{f}]\pi^+)},$$

the charge asymmetry for each final state,

$$A_h^f = \frac{\Gamma(B^- \rightarrow D[\rightarrow f]h^-) - \Gamma(B^+ \rightarrow D[\rightarrow \bar{f}]h^+)}{\Gamma(B^- \rightarrow D[\rightarrow f]h^-) + \Gamma(B^+ \rightarrow D[\rightarrow \bar{f}]h^+)},$$

and the ratio of the suppressed to favoured modes for  $D \rightarrow K\pi$  and  $D \rightarrow K\pi\pi$ ,

$$R_h^\pm = \frac{B^\pm \rightarrow D[f_{\text{sup}}]h^\pm}{B^\pm \rightarrow D[f]h^\pm}.$$

The values obtained for each of these observables can be found in Refs. [6, 7]. These variables serve as inputs for the combined  $\gamma$  measurements in Section 1.3 and Section 1.4.

## 1.2 GGSZ analysis of $B^\pm \rightarrow DK^\pm$

The GGSZ method [8] exploits the variation of the strong phase  $\delta_D$  across the Dalitz plot in  $D$  decays to three-body self-conjugate states such as  $K_S^0\pi^+\pi^-$  and  $K_S^0K^+K^-$ . The Dalitz plot is divided into bins, as shown in Fig. 4, chosen to maximise statistical sensitivity. The populations of  $B^+$  and  $B^-$  decays in each bin are given by

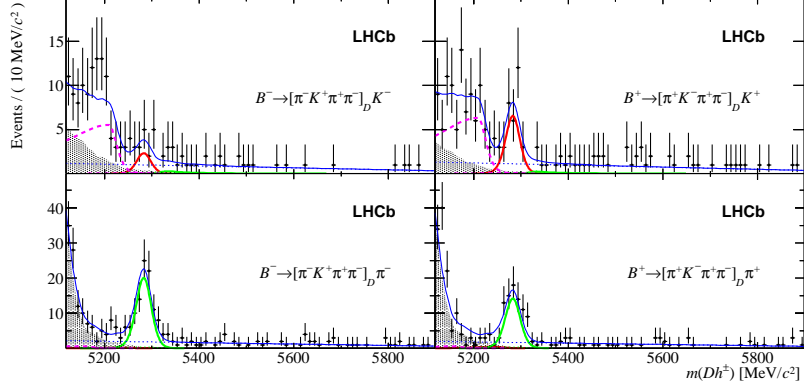


Figure 3: Fits to the invariant mass distributions of the four-body suppressed ADS mode  $\pi^\mp K^\pm \pi^\pm \pi^\mp$  in (top)  $B^\mp \rightarrow DK^\mp$  and (bottom)  $B^\mp \rightarrow D\pi^\mp$ . The  $B^\mp \rightarrow DK^\mp$  and  $B^\mp \rightarrow D\pi^\mp$  components are shown in red and green, respectively. The shaded component indicates partially reconstructed background, the dashed magenta line corresponds to partially reconstructed  $B_s^0 \rightarrow DK^- \pi^+$  and the total shape also includes a combinatoric background.

$$N_{\pm i}^+ = h_{B^+} \left[ K_{\mp i} + (x_+^2 + y_+^2) K_{\pm i} + 2\sqrt{K_i K_{-i}} (x_+ c_{\pm i} \mp y_+ s_{\pm i}) \right],$$

$$N_{\pm i}^- = h_{B^-} \left[ K_{\pm i} + (x_-^2 + y_-^2) K_{\mp i} + 2\sqrt{K_i K_{-i}} (x_- c_{\pm i} \pm y_- s_{\pm i}) \right],$$

where  $K_{\pm i}$  is the efficiency corrected yield in bin  $\pm i$  due to  $D^0$  flavour tagged events from BaBar [9, 10] and  $c_{\pm i}$  and  $s_{\pm i}$  are the cosine and sine of the strong phase  $\delta_D$  in bin  $\pm i$  from CLEO-c [11].

The remaining parameters are left free in the fit to the data:  $h_{B^\pm}$  are normalisation factors for  $B^\pm$ , and  $x_\pm = r_B \cos(\delta_B \pm \gamma)$  and  $y_\pm = r_B \sin(\delta_B \pm \gamma)$  are the Cartesian parameters, which are sensitive to  $\gamma$ .

Analyses have been performed on  $B^\pm \rightarrow DK^\pm$  with the  $D$  meson reconstructed in the final states  $K_S^0 \pi^+ \pi^-$  and  $K_S^0 K^+ K^-$  using LHCb data corresponding to  $1 \text{ fb}^{-1}$  of  $pp$  collisions at a centre of mass energy of 7 TeV [12] and  $2 \text{ fb}^{-1}$  of  $pp$  collisions at a centre of mass energy of 8 TeV [13]. The values obtained for the Cartesian parameters in the 8 TeV analysis are

$$x_+ = (-8.7 \pm 3.1(\text{stat.}) \pm 1.6(\text{syst.}) \pm 0.6(\text{ext.})) \times 10^{-2},$$

$$x_- = (5.3 \pm 3.2(\text{stat.}) \pm 0.9(\text{syst.}) \pm 0.9(\text{ext.})) \times 10^{-2},$$

$$y_+ = (0.1 \pm 3.6(\text{stat.}) \pm 1.4(\text{syst.}) \pm 1.9(\text{ext.})) \times 10^{-2},$$

$$y_- = (9.9 \pm 3.6(\text{stat.}) \pm 2.2(\text{syst.}) \pm 1.6(\text{ext.})) \times 10^{-2},$$

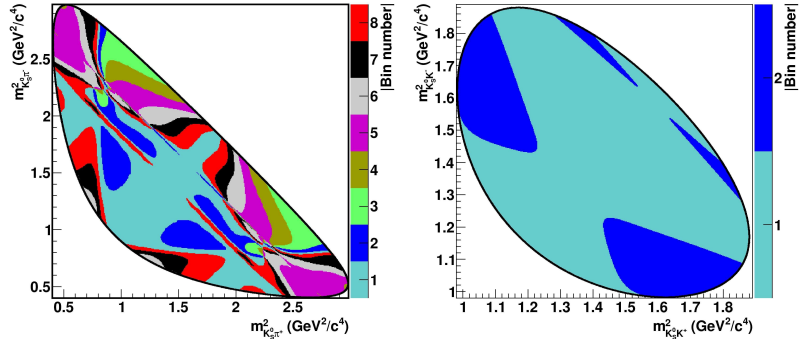


Figure 4: Binning schemes used for the Dalitz plots of (left)  $D \rightarrow K_S^0 \pi^+ \pi^-$  and (right)  $D \rightarrow K_S^0 K^+ K^-$ . Bins in the top-left half of the plots ( $m_{K_S^0 h^-}^2 > m_{K_S^0 h^+}^2$ ) are identified as  $+i$  and bins in the bottom-right half are labeled  $-i$ .

where the third uncertainty is due to the CLEO-c strong phase measurements used in the fit.

Combining these values with the results from the 7 TeV analysis and fitting for  $\gamma$ ,  $r_B$  and  $\delta_B$  yields values of  $(57 \pm 16)^\circ$ ,  $(8.8_{-2.4}^{+2.3}) \times 10^{-2}$  and  $(124_{-17}^{+15})^\circ$ , respectively, where the values for  $\gamma$  and  $\delta_B$  are modulo  $180^\circ$ . Two-dimensional projections of the confidence regions for these parameters are shown in Fig. 5.

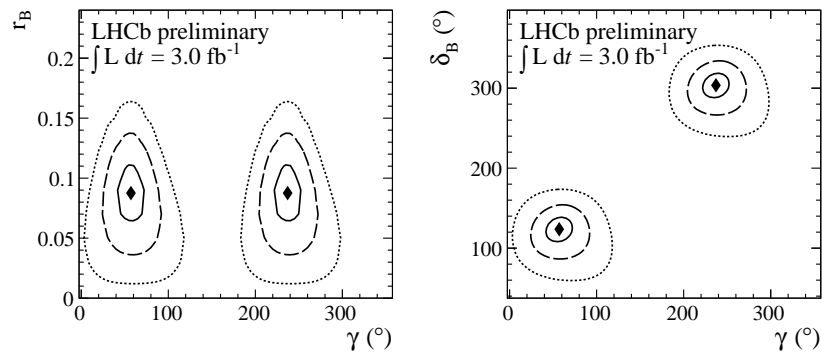


Figure 5: Two-dimensional projections of the confidence regions onto the (left)  $(\gamma, r_B)$  and (right)  $(\gamma, \delta_B)$  planes. Contours indicate the 1, 2 and  $3\sigma$  boundaries and diamonds mark the central values.

### 1.3 Combination of results from $1 \text{ fb}^{-1}$ measurements

The results in Section 1.1 and Section 1.2 are combined using a frequentist approach to obtain a more constraining measurement of  $\gamma$  [14]. In addition to these results

combination	$\gamma$	68% CL	95% CL
$DK$	$72.0^\circ$	$[56.4, 86.7]^\circ$	$[42.6, 99.6]^\circ$
$D\pi$	$18.9^\circ$	$[7.4, 99.2]^\circ \cup [167.9, 176.4]^\circ$	-
$DK$ and $D\pi$	$72.6^\circ$	$[55.4, 82.3]^\circ$	$[40.2, 92.7]^\circ$

Table 1: Best-fit values and confidence intervals for  $\gamma$  from the combination of  $DK$  and  $D\pi$  measurements.

further measurements are included to improve the fit: measurements of the strong phases and coherence factors for  $D \rightarrow K\pi$  and  $D \rightarrow K\pi\pi\pi$  decays from CLEO-c [15],  $CP$  asymmetry measurements of the neutral  $D$  mesons from the Heavy Flavour Averaging Group [16] and charm mixing parameters from LHCb [17]. A likelihood is constructed from the measured observables as

$$\mathcal{L}(\vec{\alpha}) = \prod_i \xi_i \left( \vec{A}_i^{\text{obs}} | \vec{\alpha} \right),$$

where the sum is over the different measurements,  $\vec{\alpha}$  is the set of parameters and  $\xi_i$  denotes the likelihood probability density functions (PDFs) of the observables  $\vec{A}_i^{\text{obs}}$ . For most observables a Gaussian PDF is assumed, however, where highly non-Gaussian behaviour is observed, the experimental likelihood is used.

A combined  $\gamma$  measurement has been performed including the results from Section 1.1 and a subset of the results from Section 1.2 corresponding to  $1 \text{ fb}^{-1}$  of  $pp$  collisions at a centre of mass energy of 7 TeV [12]. The best-fit values and confidence intervals (modulo  $180^\circ$ ) of  $\gamma$  are given in Table 1 and the  $1 - \text{CL}$  curves for  $\gamma$  are shown in Fig. 6.

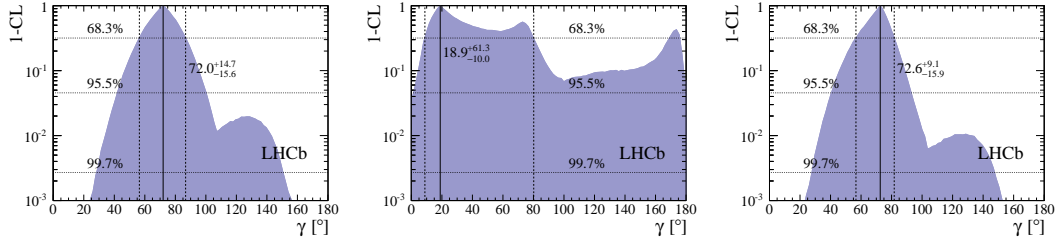


Figure 6:  $1 - \text{CL}$  curves for  $\gamma$  from the combined  $1 \text{ fb}^{-1}$  GLW/ADS and  $1 \text{ fb}^{-1}$  GGSZ measurements using (left) only  $DK$ , (centre) only  $D\pi$  and (right) both decay modes.

#### 1.4 Combination including $3 \text{ fb}^{-1}$ GGSZ measurement

Another combination [18] has been performed that incorporates all of the results reported in Section 1.2 but only those observables from Section 1.1 corresponding

quantity	value	68 % CL	95 % CL
$\gamma$	$67.2^\circ$	$[55.1, 79.1]^\circ$	$[43.9, 89.5]^\circ$
$r_B$	0.0923	$[0.0843, 0.1001]$	$[0.0762, 0.1075]$
$\delta_B$	$114.3^\circ$	$[101.3, 126.3]^\circ$	$[88.7, 136.3]^\circ$

Table 2: Best-fit values and confidence intervals for  $\gamma$ ,  $r_B$  and  $\delta_B$  from the combination of  $DK$  measurements including GGSZ measurements from  $3 \text{ fb}^{-1}$  of data.

to  $B^\pm \rightarrow DK^\pm$  decays. Mixing in the neutral  $D$  mesons is also neglected in the equations used for the observables in this combination.

The best-fit values and confidence intervals (all modulo  $180^\circ$ ) for  $\gamma$ ,  $r_B$  and  $\delta_B$  are given in Table 2. Figure 7 and Figure 8 show the  $1 - \text{CL}$  curve for  $\gamma$ , and the 2D projection of the likelihood in  $\gamma$  and  $r_B$ , respectively.

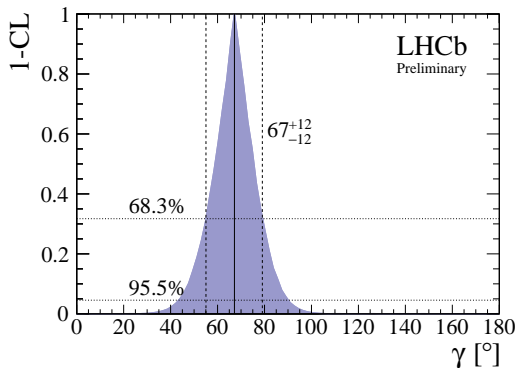


Figure 7:  $1 - \text{CL}$  curve for  $\gamma$  from the combined  $1 \text{ fb}^{-1}$  GLW/ADS and  $3 \text{ fb}^{-1}$  GGSZ measurements.

## 2 Measurement of $B_{(s)}^0 \rightarrow DK\pi$ branching fractions

The decay mode  $B^0 \rightarrow DK^+\pi^-$  has potential for a significant future measurement of  $\gamma$  [19–21]. Sensitivity to  $\gamma$  comes from the interference of  $b \rightarrow c$  and  $b \rightarrow u$  amplitudes of a similar magnitude.  $B_s^0 \rightarrow DK^-\pi^+$  and the related mode  $B_s^0 \rightarrow D^*K^-\pi^+$  form important backgrounds to this mode, therefore, an understanding of these modes is necessary.

Branching fraction measurements of  $B^0 \rightarrow DK^+\pi^-$  and  $B_s^0 \rightarrow DK^-\pi^+$ , relative to the normalisation mode  $B^0 \rightarrow D\pi^+\pi^-$ , have been made using LHCb data corresponding to  $1 \text{ fb}^{-1}$  of  $pp$  collisions at a centre of mass energy of 7 TeV [22].

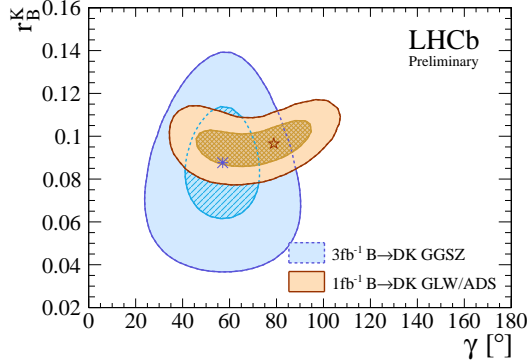


Figure 8: Two-dimensional projection of the confidence regions onto the  $(\gamma, r_B)$  plane. Contours show the 1 and  $2\sigma$  boundaries and markers indicate the central values.

The invariant mass distributions of  $D\pi\pi$  and  $DK\pi$  candidates where the  $D$  is reconstructed from  $\bar{D}^0 \rightarrow K^+\pi^-$  are shown in Fig. 9. The measured relative branching fractions are

$$\frac{\mathcal{B}(B^0 \rightarrow \bar{D}^0 K^+ \pi^-)}{\mathcal{B}(B^0 \rightarrow \bar{D}^0 \pi^+ \pi^-)} = 0.106 \pm 0.007 (\text{stat.}) \pm 0.008 (\text{syst.}),$$

$$\frac{\mathcal{B}(B_s^0 \rightarrow \bar{D}^0 K^- \pi^+)}{\mathcal{B}(B^0 \rightarrow \bar{D}^0 \pi^+ \pi^-)} = 1.18 \pm 0.05 (\text{stat.}) \pm 0.12 (\text{syst.}).$$

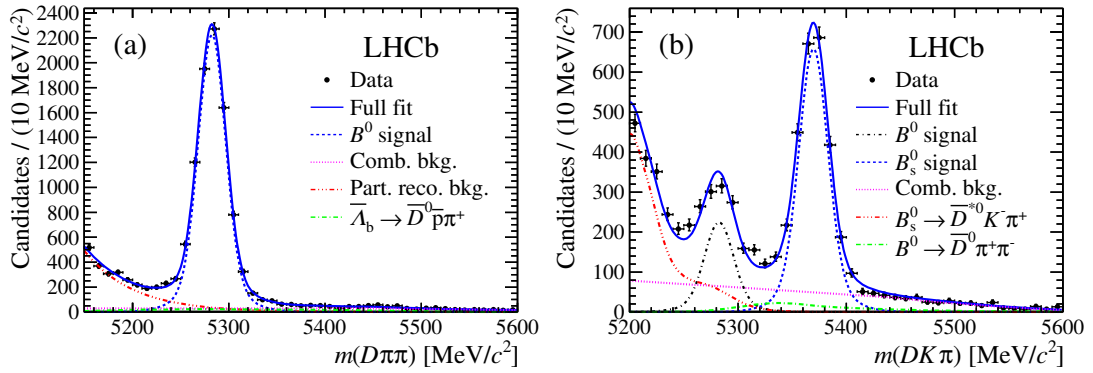


Figure 9: Fits to the  $B_{(s)}^0$  candidate invariant mass distributions for the (a)  $D\pi\pi$  and (b)  $DK\pi$  samples. Data points are shown in black, the full fitted PDFs as solid blue lines and the components as detailed in the legends.



These relative measurements yield absolute branching fractions of

$$\mathcal{B}(B^0 \rightarrow \bar{D}^0 K^+ \pi^-) = (9.0 \pm 0.6 \text{ (stat.)} \pm 0.7 \text{ (syst.)} \pm 0.9(\mathcal{B})) \times 10^{-5},$$

$$\mathcal{B}(B_s^0 \rightarrow \bar{D}^0 K^- \pi^+) = (1.00 \pm 0.04 \text{ (stat.)} \pm 0.10 \text{ (syst.)} \pm 0.10(\mathcal{B})) \times 10^{-3},$$

where the third uncertainty arises from the uncertainties on  $\mathcal{B}(B^0 \rightarrow \bar{D}^0 \pi^+ \pi^-)$ . This is the most precise measurement of  $\mathcal{B}(B^0 \rightarrow \bar{D}^0 K^+ \pi^-)$  to date and the first measurement of  $\mathcal{B}(B_s^0 \rightarrow \bar{D}^0 K^- \pi^+)$ .

Although no quantitative analysis of the Dalitz plots has yet been attempted, the Dalitz plot distributions obtained (corrected for efficiency) are presented in Fig. 10.

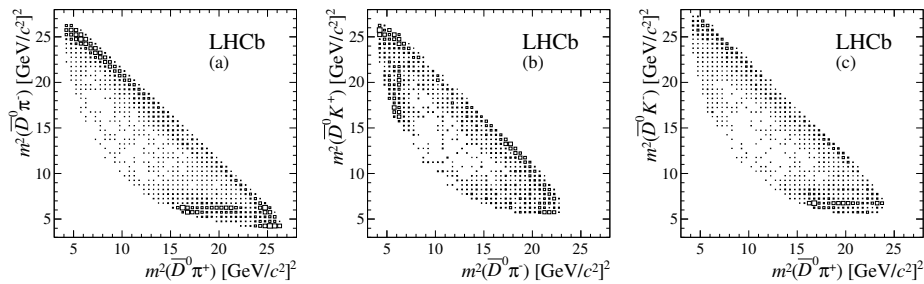


Figure 10: Efficiency corrected Dalitz plot distributions for (a)  $B^0 \rightarrow \bar{D}^0 \pi^+ \pi^-$ , (b)  $B^0 \rightarrow \bar{D}^0 K^+ \pi^-$  and (c)  $B_s^0 \rightarrow \bar{D}^0 K^- \pi^+$  candidates obtained from the signal weights.

### 3 Conclusions and prospects

The  $B^\pm \rightarrow DK^\pm$  decay mode offers an excellent opportunity to measure the CKM angle  $\gamma$  from Standard Model processes. The combination in Section 1.4 gives the most sensitive measurement of  $\gamma$  from a single experiment so far, yielding a value of  $(67 \pm 12)^\circ$ . This measurement is expected to improve further with the completion of a GLW/ADS analysis on the remaining  $2 \text{ fb}^{-1}$  of LHCb data currently available. In addition, other modes such as  $B^0 \rightarrow DK^+ \pi^-$  offer great prospects for future  $\gamma$  measurements.

### ACKNOWLEDGMENTS

This work is funded in part by the European Research Council under FP7 and by the United Kingdom's Science and Technology Facilities Council.

## References

- [1] K. Trabelsi [Belle Collaboration], arXiv:1301.2033 [hep-ex].
- [2] J. P. Lees *et al.* [BaBar Collaboration], Phys. Rev. D **87** (2013) 052015 [arXiv:1301.1029 [hep-ex]].
- [3] J. Charles *et al.* [CKMfitter Group Collaboration], Eur. Phys. J. C **41** (2005) 1 [hep-ph/0406184].
- [4] M. Gronau and D. Wyler, Phys. Lett. B **265** (1991) 172.
- [5] D. Atwood, I. Dunietz and A. Soni, Phys. Rev. Lett. **78** (1997) 3257 [hep-ph/9612433].
- [6] R. Aaij *et al.* [LHCb Collaboration], Phys. Lett. B **712** (2012) 203 [Erratum-ibid. B **713** (2012) 351] [arXiv:1203.3662 [hep-ex]].
- [7] R. Aaij *et al.* [LHCb Collaboration], Phys. Lett. B **723** (2013) 44 [arXiv:1303.4646 [hep-ex]].
- [8] A. Giri, Y. Grossman, A. Soffer and J. Zupan, Phys. Rev. D **68** (2003) 054018 [hep-ph/0303187].
- [9] B. Aubert *et al.* [BaBar Collaboration], Phys. Rev. D **78** (2008) 034023 [arXiv:0804.2089 [hep-ex]].
- [10] P. del Amo Sanchez *et al.* [BaBar Collaboration], Phys. Rev. Lett. **105** (2010) 121801 [arXiv:1005.1096 [hep-ex]].
- [11] J. Libby *et al.* [CLEO Collaboration], Phys. Rev. D **82** (2010) 112006 [arXiv:1010.2817 [hep-ex]].
- [12] R. Aaij *et al.* [LHCb Collaboration], Phys. Lett. B **718** (2012) 43 [arXiv:1209.5869 [hep-ex]].
- [13] R. Aaij *et al.* [LHCb Collaboration], LHCb-CONF-2013-004 (2013).
- [14] R. Aaij *et al.* [LHCb Collaboration], arXiv:1305.2050 [hep-ex].
- [15] N. Lowrey *et al.* [CLEO Collaboration], Phys. Rev. D **80** (2009) 031105 [arXiv:0903.4853 [hep-ex]].
- [16] Y. Amhis *et al.* [Heavy Flavor Averaging Group Collaboration], arXiv:1207.1158 [hep-ex].

- [17] R. Aaij *et al.* [LHCb Collaboration], Phys. Rev. Lett. **110** (2013) 101802 [arXiv:1211.1230 [hep-ex]].
- [18] R. Aaij *et al.* [LHCb Collaboration], LHCb-CONF-2013-006 (2013).
- [19] M. Gronau, Phys. Lett. B **557** (2003) 198 [hep-ph/0211282].
- [20] T. Gershon, Phys. Rev. D **79** (2009) 051301 [arXiv:0810.2706 [hep-ph]].
- [21] T. Gershon and M. Williams, Phys. Rev. D **80** (2009) 092002 [arXiv:0909.1495 [hep-ph]].
- [22] R. Aaij *et al.* [LHCb Collaboration], Phys. Rev. D **87** (2013) 112009 [arXiv:1304.6317 [hep-ex]].